JACS
JOURNAL OF THE AMERICAN CHEMICAL SOCIETY
Article
pubs.acs.org/JACS

Unravelling the Effects of Grain Boundary and Chemical Doping on Electron−Hole Recombination in $CH_3NH_3PbI_3$ Perovskite by Time-Domain Atomistic Simulation

Run Long,*[,†,‡] Jin Liu,[§] and Oleg V. Prezhdo*[,∥]

[†]College of Chemistry, Key Laboratory of Theoretical & Computational Photochemistry of Ministry of Education, Beijing Normal University, Beijing 100875, P. R. China

[‡]School of Physics, Complex & Adaptive Systems Lab, University College Dublin, Dublin 4, Ireland

[§]Department of Chemical Engineering, University of Rochester, Rochester, New York 14627, United States

[∥]Department of Chemistry, University of Southern California, Los Angeles, California 90089, United States

ABSTRACT: Advancing organohalide perovskite solar cells requires understanding of carrier dynamics. Electron−hole recombination is a particularly important process because it constitutes a major pathway of energy and current losses. Grain boundaries (GBs) are common in methylammonium lead iodine $CH_3NH_3PbI_3$ ($MAPbI_3$) perovskite polycrystalline films. First-principles calculations have suggested that GBs have little effect on the recombination; however, experiments defy this prediction. Using nonadiabatic (NA) molecular dynamics combined with time-domain density functional theory, we show that GBs notably accelerate the electron−hole recombination in $MAPbI_3$. First, GBs enhance the electron−phonon NA coupling by localizing and contributing to the electron and hole wave functions and by creating additional phonon modes that couple to the electronic degrees of freedom. Second, GBs decrease the $MAPbI_3$ bandgap, reducing the number of vibrational quanta needed to accommodate the electronic energy loss. Third, the phonon-induced loss of electronic coherence remains largely unchanged and not accelerated, as one may expect from increased electron−phonon coupling. Further, replacing iodines by chlorines at GBs reduces the electron−hole recombination. By pushing the highest occupied molecular orbital (HOMO) density away from the boundary, chlorines restore the NA coupling close to the value observed in pristine $MAPbI_3$. By introducing higher-frequency phonons and increasing fluctuation of the electronic gap, chlorines shorten electronic coherence. Both factors compete successfully with the reduced bandgap relative to pristine $MAPbI_3$ and favor long excited-state lifetimes. The simulations show excellent agreement with experiment and characterize how GBs and chlorine dopants affect electron−hole recombination in perovskite solar cells. The simulations suggest a route to increased photon-to-electron conversion efficiencies through rational GB passivation.

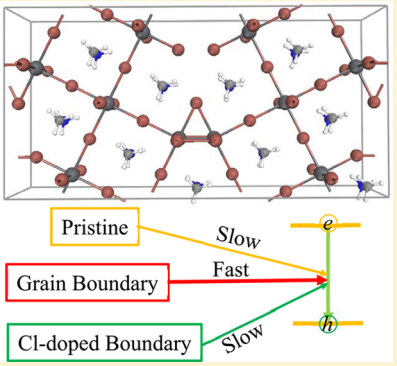

1. INTRODUCTION

Hybrid organic−inorganic perovskite solar cells have attracted great attention due to the high power conversion efficiencies reaching[1−10] and exceeding[11,12] 20%. The remarkable performance stems from large carrier lifetimes and long carrier diffusion lengths.[13−15] The bandgap of lead halide perovskites $CH_3NH_3PbI_3$ ($MAPbI_3$) is suitable to harvest both visible and near-infrared parts of the solar spectrum. In addition to the excellent photovoltaic properties, these materials are also known for high photoluminescence quantum yields.[16,17] Recently, $MAPbI_3$ applications have extended into other areas, including light-emitting diodes,[18] optically pumped lasers,[17,19] and photo- and electrocatalytic water-splitting assemblies.[20,21] To achieve high performance of solar cells and other optoelectronic devices, slow nonradiative electron−hole recombination is required, because it constitutes a major pathway for charge and energy losses.

Halide perovskite thin films obtained from low-temperature thermal evaporation and solution-based processing are polycrystalline.[22] Therefore, grain boundaries (GBs) unavoidably exist in the samples. Charges generated in $MAPbI_3$ by photoexcitation exhibit extremely long diffusion lengths, on the order of 100 nm.[15] Doping by chlorines increases diffusion lengths of both electron and hole up to 1 μm.[14] Single-crystalline $MAPbI_3$ demonstrates diffusion lengths exceeding 175 μm.[13] The large photoexcited-state lifetimes and extremely long charge diffusion lengths indicate that charges encounter GBs before recombination. This raises the question of how the local microstructure affects the electron−hole recombination.

First-principles calculations have suggested that $MAPbI_3$ GBs are benign.[23,24] However, experimental works have shown that GBs notably affect the film optoelectronic properties.[25−29] Tosun and Hillhouse have demonstrated that grain size can be increased significantly by annealing perovskite films in the presence of MAI vapor.[27] The annealed films have exhibited

Received: January 19, 2016
Published: March 1, 2016

DOI: 10.1021/jacs.6b00645
J. Am. Chem. Soc. 2016, 138, 3884−3890

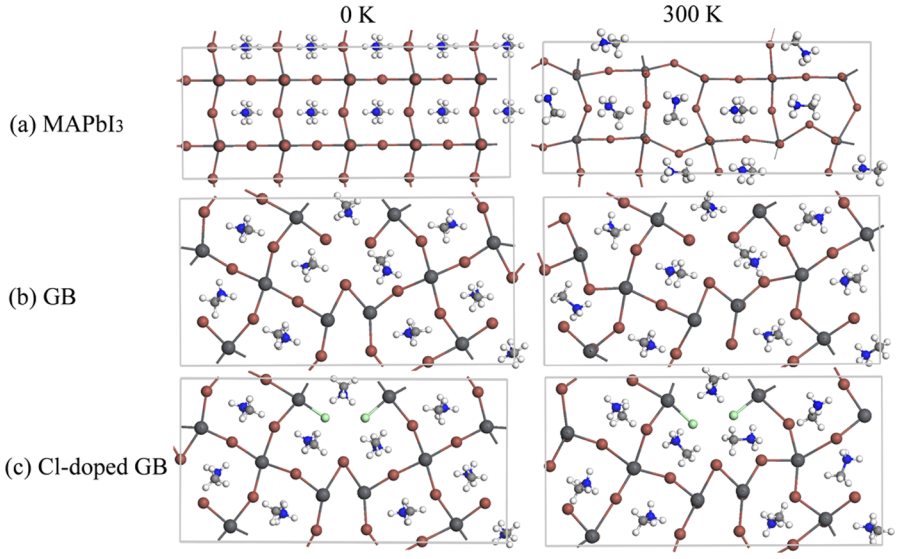

Figure 1. Simulation cell showing the geometry of (a) 1 × 2 × 5 120-atom ideal $MAPbI_3$, (b) 120-atom Σ5 (012) grain boundary (GB) structure, and (c) Cl-doped Σ5 (012) GB structure. The structures shown at 0 K (left panel) and 300 K (right panel) demonstrate that thermal atomic motions alter the geometries, and hence, modulate the electron−hole interaction.

much longer excited-state lifetimes. Xiao and coauthors have demonstrated that annealing in the presence of solvent vapor increases grain size in perovskite films, which show better solar cells performance than the initial films.[29] Nie et al. have also shown that the improved perovskite solar cells performance can be attributed to the increased grain size and reduced bulk defects.[28] They have further shown that large-grained perovskite films exhibit higher carrier mobilities and longer electron−hole recombination times than the small-grained films.[28] Similarly, Bischak et al. have reported significant differences in nonradiative recombination rates from grain to grain within $MAPbI_3$ films using cathodoluminescence microscopy.[25] These observations suggest that GBs accelerate electron−hole recombination and that the negative influence can be minimized by reducing GBs and creating large-scale grained films.

Recently, Stranks and coauthors have demonstrated using confocal fluorescence microscopy correlated with scanning electron microscopy[26] that the electron−hole recombination rate is greatly reduced in the presence of GBs, while it is increased with Cl doping, This experiment explicitly suggests that GBs are detrimental to solar cell performance due to accelerated electronic energy loss to heat. To clarify the role of GBs and GB doping on the electron−hole recombination within $MAPbI_3$ perovskites, a real-time atomistic simulation is needed to mimic the electronic-vibrational dynamics directly as they occur in experiments.

Motivated by the recent experimental works,[25−29] we report an ab initio atomistic time-domain[30] study of the influence of GBs and Cl doping on electron−hole recombination in $MAPbI_3$ and provide guidelines for minimizing energy losses. The study shows that nonradiative electron−hole recombination in pristine $MAPbI_3$ occurs within tens of picoseconds, agreeing well with both experimental data[31−34] and previous simulation on tetragonal $MAPbI_3$.[35] Most importantly, we demonstrate that GBs strongly accelerate the recombination, while introduction of substitutional Cl dopants at the boundary reduces the recombination, making it even slower than in the pristine system. The presence of GBs notably accelerates charge and energy losses for several reasons. GBs increase the electron−phonon nonadiabatic (NA) couplings between the lowest unoccupied molecular orbital (LUMO) and the highest occupied molecular orbital (HOMO). The coupling is enhanced in particular because HOMO becomes localized at the GB and shows stronger dependence on nuclear displacements. $MAPbI_3$ containing GBs reduces the bandgap, bringing the electronic and vibrational quanta closer to resonance. At the same time, phonon-induced decay of quantum coherence between HOMO and LUMO remains largely unchanged, because no foreign light atoms are incorporated into the lattice. Once lighter Cl substitutes heavier I at a GB, it introduces higher-frequency vibrations and accelerates quantum coherence loss. Further, in contrast to I, the Cl dopant does not contribute to the hole wave function, eliminating some of the needed wave function overlap and reducing the electron−phonon NA coupling. Both factors compete successfully with the reduced bandgap relative to pristine $MAPbI_3$. As a result, the electron−hole recombination is suppressed in $MAPbI_3$ with Cl-doped GBs. The latter finding suggests a route for improving performance of perovskite materials by adding Cl dopants during GB annealing.

2. SIMULATION METHODOLOGY

NA molecular dynamics (NA-MD)[36] are carried out by the mixed quantum-classical fewest switching surface hopping (FSSH)[37] technique implemented within the time-dependent Kohn−Sham density functional theory (DFT).[38−41] The lighter and faster electrons are treated quantum mechanically, while the heavier and slower nuclei are described classically. The approach provides a detailed ab initio description of coupled electron-vibrational dynamics[42] in real time and satisfies the closely detailed balance between transitions upward and downward in energy.[43] A semiclassical correction for quantum decoherence,[19,44−46] known as pure dephasing in the optical-response theory,[47] is used, because the decoherence time is significantly shorter than the quantum transition time. The approach has been applied to study excitation dynamics in a broad range of systems.[35,48−58]

Geometry optimization, adiabatic MD, and NA couplings calculations are carried using the Vienna ab initio simulation package (VASP).[59] The exchange-correlation interactions are treated using the Pedrew−Burke−Ernzerhof (PBE) functional.[60] The interaction between the ionic cores and the valence electrons are described by

DOI: 10.1021/jacs.6b00645
J. Am. Chem. Soc. 2016, 138, 3884−3890

the projector-augmented wave (PAW) approach.[61] Pure DFT functionals, such as PBE, produce good values for the bandgap of hybrid perovskites due to a cancelation of two effects.[62,63] On the one hand, lead is a heavy element requiring incorporation of spin−orbit interactions, which typically increase the gap. On the other hand, pure DFT functionals underestimate gaps due to the self-interaction error. Relativistic and hybrid functionals introduce significant computational expense and cannot be used in the current simulation, because NA-MD requires thousands of electronic structure calculations for every step along the trajectories. The van der Waals interactions are treated by the Grimme DFT-D2 method.[64]

After relaxing the geometry at 0 K, the three systems have been heated to 300 K using velocity rescaling. Then, 4 ps adiabatic MD trajectories have been generated in the microcanonical ensemble with a 1 fs atomic time-step. To simulate the electron−hole recombination, 1000 geometries have been selected randomly from the adiabatic MD trajectories. They have been used as initial conditions for NA-MD simulations. A detailed description of the method and its implementation can be found elsewhere.[40,41]

The pseudocubic phase[65] of $MAPbI_3$ with the optimized lattice constant of 6.29 Å has been used to create the Σ5(012) GB structure containing 120 atoms (Figure 1b). To create a Cl-doped Σ5(012) GB, two iodine atoms belonging to the GB have been replaced by two Cl atoms. This substitution has the smallest formation energy, in excellent agreement with the previous first-principles calculations.[24] To compare directly the Σ5(012) GB with and without Cl doping to pristine $MAPbI_3$, we have built the same size (1 × 2 × 5) 120-atom supercell (Figure 1a). It should be noted that it is impossible to construct identical small supercells with and without GBs. A reasonable supercell size is important for modeling electron-vibrational relaxation dynamics, because the NA-MD coupling calculations are computationally expensive.

3. RESULTS AND DISCUSSION

3.1. Geometric Structure. Figure 1 shows the optimized geometries of pristine $MAPbI_3$, $MAPbI_3$ with a GB, and a Cl-doped GB. In addition to the 0 K geometries, the figure presents snapshots of the corresponding structures from the MD trajectory at 300 K. Pristine $MAPbI_3$ shows that at 0 K the organic groups align along the <111> direction within the inorganic cages (left panel of Figure 1a). This arrangement allows hydrogens to approach iodines, form hydrogen bonds, and stabilize the organic−inorganic hybrid structure. At the ambient temperature, the organic groups rotate, and the inorganic cages distort significantly. Hydrogens approach iodines in some cases, enhancing the interaction (right panel of Figure 1a). The rotation of the organic groups has been reported by several groups,[66] including ours,[54] based on ground-state MD simulations and experimental measurements.[67,68]

Figure 1b demonstrates the optimized structure of the Σ5 (012) GB system at 0 K (left panel) and one trajectory snapshot at the ambient temperature (right panel). The GB is stable during the MD simulation at room temperature. Comparing the optimized geometries of the GB and pristine $MAPbI_3$, we observe that the orientation of the MA^+ organic cations is much more random in the presence of the boundary. This behavior allows some hydrogens to closely approach iodines, especially the uncoordinated iodine atoms of the GB. This phenomenon persists at room temperature, and some of the I−Pb bonds shorten, while others elongate. Fluctuations of the I−Pb bond lengths modify the chemical bonding of the inorganic cage further, affecting the electrostatic interaction.

Replacing the two most reactive iodine atoms of the GB with chlorines causes little distortion in the Σ5(012) GB geometry (Figure 1c). Considering the optimized geometries of the original and Cl-doped GBs (left panels of Figure 1b and c), we observe that the distances between the hydrogen atoms and the two Cl dopants are larger than between the hydrogen atoms and the original iodines. This is because the Cl radius is smaller than the I radius. On the other hand, the electronegativity of Cl (3.16) is larger than that of I (2.66).[64] As a result, Cl interacts more strongly with the organic $CH_3NH_3PbI_3$ ions than I, and the Cl atoms are pulled out away from the Pb atoms. This situation holds at both 0 K and room temperature (left and right panels of Figure b and c). Replacing iodines with chlorines at the GB decreases the electron−hole NA coupling (Table 1). This is because the band edge state of the hole, i.e., HOMO, is formed predominantly by iodine atoms (Figures 2 and 3), while chlorines do not contribute to this state.[35,54]

Table 1. Bandgap, Average NA Coupling, Pure-Dephasing Time (T_2^*), and Nonradiative Electron−Hole Recombination Time for Ideal Cubic $MAPbI_3$ at the R Point and for Σ5 (012) GB with and without Cl Doping at the M Point

	bandgap (eV)	NA coupling (meV)	dephasing (fs)	recombination (ps)
ideal	1.74	0.76	3.6	49.0/44.2[a]
Σ5 (012) GB	0.73	1.39	3.3	10.4
Cl-doped GB	0.77	0.72	1.6	68.5

[a]Electron−hole recombination time scale corresponds to the experimental bandgap of 1.55 eV for cubic $MAPbI_3$.

3.2. Electronic Structure. Figure 2 presents the density of states (DOS) and band structure of pristine $MAPbI_3$, as well as those of the original and Cl-doped Σ5(012) GBs, calculated at 0 K using the optimized structures. The DOS of pristine

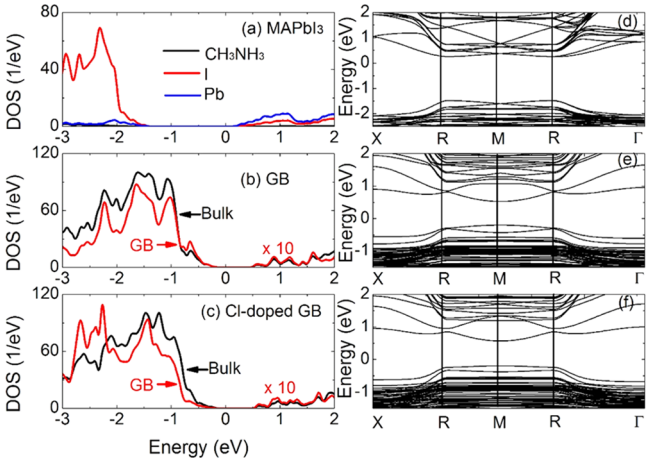

Figure 2. Density of states (DOS) and band structure of (a, d) $MAPbI_3$, (b, e) Σ5 (012) GB, and (c, f) Cl-doped Σ5 (012) GB, obtained using optimized zero-temperature geometries. The contribution of the GB atoms to DOS is magnified 10 times. Zero energy is set to the Fermi level. The DOS of pristine $MAPbI_3$ shows that LUMO is formed by Pb orbitals and HOMO is due to I and Pb orbitals. Neither GB nor Cl-doped GB create impurity states inside the bandgap. Rather, they reduce the bandgap. The GB Pb and I atoms contribute significantly to both HOMO and LUMO in the Σ5 (012) GB system. In comparison, refs 35 and 54 demonstrated that Cl dopant contributes little to HOMO. All three systems exhibit direct bandgaps located at the R-point for cubic $MAPbI_3$ and at the M-point for the GB and Cl-doped GB systems.

DOI: 10.1021/jacs.6b00645
J. Am. Chem. Soc. 2016, 138, 3884−3890

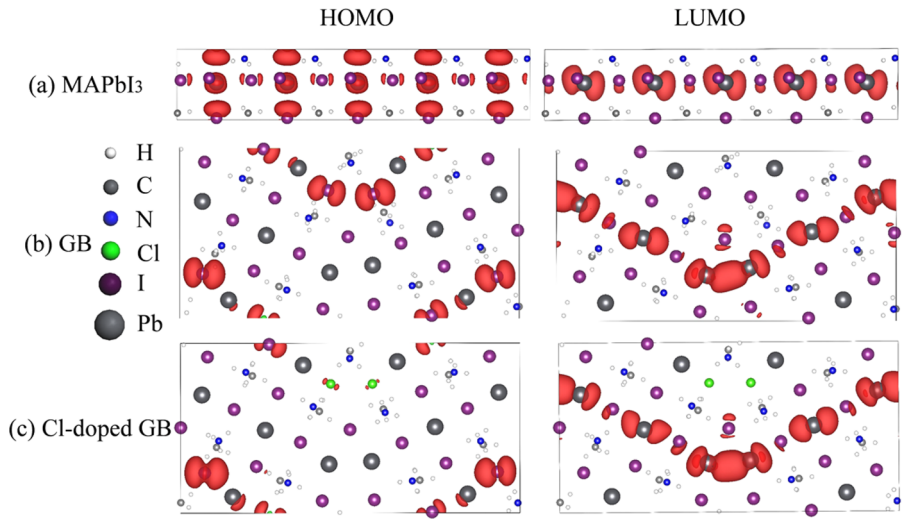

Figure 3. HOMO and LUMO charge density in (a) $MAPbI_3$, (b) Σ5 (012) GB, and (c) Cl-doped Σ5 (012) GB. HOMO and LUMO are delocalized in (a), whereas HOMO and LUMO localize on iodine and lead atoms in the vicinity of GB in (b) and (c). In the doped system, Cl contributes to HOMO less than I, as shown in refs 35 and 54.

$MAPbI_3$ is split into the CH_3NH_3, I, and Pb contributions (Figure 2a). It shows that HOMO is composed mostly by orbitals of I atoms, while LUMO arises largely due to Pb atoms. The organic groups do not contribute to the band edge states, and therefore, they have no direct effect on the NA coupling. The state densities shown in Figure 3 confirm this conclusion. LUMO and HOMO of pristine $MAPbI_3$ are separated by a wide energy gap of 1.74 eV (Table 1). This electronic energy is accommodated by phonons during the nonradiative electron−hole recombination. The gap value obtained with the PBE functional[60] shows good agreement with the previous DFT calculations and the experimental bandgap of 1.69 eV for cubic $MAPbI_3$.[69−71] Note that another experiment reported a 1.55 eV bandgap for cubic $MAPbI_3$.[65] The agreement stems from cancellation of DFT errors, which arise due to an approximate description of electron exchange-correlation and lack of relativistic effects, as demonstrated by several groups.[63,72,73]

The bandgap is greatly reduced for the Σ5(012) GBs, both with and without Cl doping (Table 1 and Figure 2b,c). The figures show the total DOS and the contribution of the GBs atoms. The latter is magnified 10 times. The GBs create no deep gap states in either system. Typically, smaller bandgaps favor electron−hole recombination, because they bring the electronic and vibrational quanta closer to resonance. Figure 2b indicates that GB atoms contribute significantly to HOMO and LUMO. Both orbitals, and especially HOMO, are localized at the boundary, as shown explicitly in Figure 3b. Introduction of chlorines into the Σ5(012) GB system has little effect on LUMO (Figures 2c and 3c). However, HOMO is affected strongly. Chlorine atoms contribute little to either HOMO or LUMO (Figure 3c). This fact also holds for a perfect $MAPbI_3$ surface.[35,54] By replacing iodines, chlorines reduce the GB contribution to DOS at the valence band edge; compare parts b and c of Figure 2. Because the wave functions of chlorine atoms do not contribute to the NA coupling between the band edge states, the coupling decreases upon the GB doping (Table 1).

The calculated band structures for the three systems shown in Figure 2d,e confirm the conclusions drawn from the DOS analysis: the GBs do not generate deep trap states. The band structures further reveal a direct bandgap at the high-symmetry R point for pristine $MAPbI_3$. The gap shifts to the M point for the Σ5(012) GBs system with and without Cl doping. The bandgaps summarized in Table 1 demonstrate that Cl doping leads to a slight reduction of the bandgap relative to the undoped Σ5(012) GB system, 0.73 vs 0.77 eV.

In addition to the electronic bandgap, the electron−hole recombination rate depends on the NA coupling between the initial and finial state. The strength of the coupling is related to the corresponding wave function overlap. Shown in Figure 3a for the pristine $MAPbI_3$ system, HOMO is localized primarily on iodine atoms and is slightly delocalized onto leads. LUMO is formed by lead atoms. This conclusion is consistent with the DOS analysis (Figure 2a). HOMO of the Σ5(012) GBs system is mainly localized on the iodine atoms of the GB (Figure 3b). The corresponding LUMO is primarily distributed on the middle row of lead atoms, with the lead atoms of the GB having the largest contribution. By visually evaluating the HOMO−LUMO overlap, which appears largest for pristine $MAPbI_3$ (Figure 3), one may assume that the NA coupling is larger for the pristine system than for the GB systems. This is not the case, however (Table 1). The NA couplings of all three systems are very small, on the order of 1 meV, compared to other systems studied in our group.[48−50,54] Indeed, HOMO and LUMO of the GB systems show little overlap according to Figure 3b,c. The NA coupling in pristine $MAPbI_3$ is small due to wave function symmetries and NA coupling selection rules. The charge densities, shown in Figure 3 for all three systems, are consistent with DOS presented in Figure 2.

3.3. Electron-Vibrational Interactions. Electron-vibrational interactions are responsible for elastic and inelastic electron−phonon scattering. Both types of scattering affect the excited-state lifetime. Inelastic energy exchange between the electronic and vibrational degrees of freedom is required to accommodate the energy lost during the electronic transition from LUMO to HOMO. Elastic electron−phonon scattering destroys coherence formed between LUMO and HOMO when they become coupled by the NA interaction during the nonradiative relaxation. Elastic electron−phonon scattering is known in optical measurements as pure dephasing.[47]

Figure 4 presents Fourier transforms (FTs) of the HOMO−LUMO energy gaps in the three systems. FT characterizes the phonon modes that couple to the electronic degrees of

DOI: 10.1021/jacs.6b00645
J. Am. Chem. Soc. 2016, 138, 3884−3890

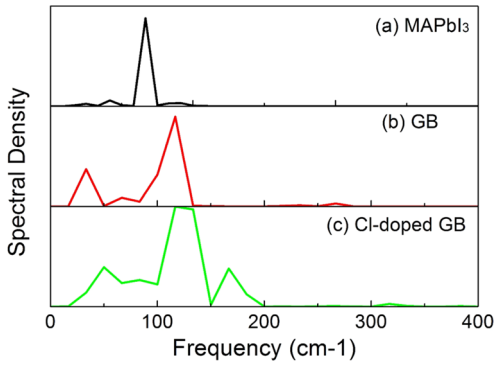

Figure 4. Fourier transforms of autocorrelation functions for the HOMO−LUMO gap in (a) $MAPbI_3$, (b) Σ5 (012) GB, and (c) Cl-doped Σ5 (012) GB.

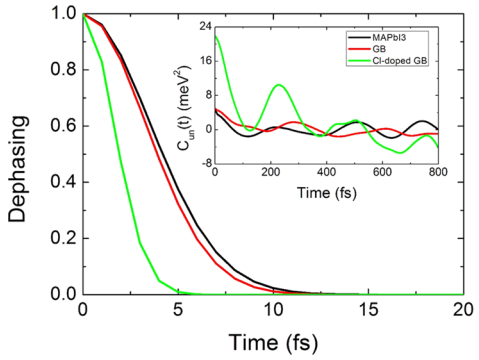

Figure 5. Pure-dephasing functions for the HOMO−LUMO transition in the three systems. The decay time scale represents the elastic electron−phonon scattering time. The data are fitted by Gaussians, and the pure-dephasing times are given in Table 1. The inset shows the unnormalized autocorrelation function. The initial value represents the bandgap fluctuation squared. Typically,[75] the bigger the fluctuation, the faster is the dephasing.

freedom, induce decoherence, and accommodate the excess energy dissipated during electron−hole recombination. Only low-frequency vibrations participate in the nonradiative decay in all three cases. By breaking the perfect crystal symmetry, the GB relaxes the coupling selection rules, allowing higher frequency modes to participate in the electron−hole recombination process. The Cl dopants increase the range of active vibration frequencies further, since they are lighter than the I atoms they replace.

The dominant peak in pristine $MAPbI_3$ can be assigned[74] to the Pb−I bond stretching at 94 cm^{-1}. This frequency is the diagnostic mode of the inorganic cage. The peak at 119 cm^{-1}, attributed[74] to librations of the organic cations, contributes very little to the signal, in particular because neither HOMO nor LUMO delocalize onto these moieties (Figure 2a). The side peak below the main frequency can be assigned[74] to the Pb−I bond bending mode at 62 cm^{-1}. Both Pb−I stretching and bending modes alter the $MAPbI_3$ geometry, create the NA coupling, and lead to electron−hole recombination. Because of symmetry breaking upon introduction of the Σ5(012) GB, the main peak splits into two peaks. Chlorine doping introduces a fairly broad range of modes capable of interacting with the electronic subsystem. FTs of the energy gaps presented in Figure 4 are directly related to the pure-dephasing function (Figure 5). Higher peak intensities and a broader range of frequencies point to faster dephasing (Table 1).

The optical pure-dephasing functions, computed using the second-order cumulant approximation,[75] are shown in Figure 5. The functions characterize elastic electron−phonon scattering. The dephasing times, τ, summarized in Table 1, were obtained by fitting the functions to a Gaussian, $\exp[-0.5(t/\tau)^2]$. The pure-dephasing times are very short, 3.6, 3.3, and 1.6 fs. They decrease from pristine $MAPbI_3$, to the GB, to the Cl-doped GB. The mild decrease from pristine $MAPbI_3$ to the GB can be attributed to participation of the second phonon (Figure 4b), due to breaking of the perfect symmetry by the GB. The factor of 2 drop in the pure-dephasing time for the chlorine-doped GB arises from participation of a broad range of phonons, several of which exhibit high intensity (Figure 4c). The elastic electron−phonon scattering time for the electron−hole recombination process is much shorter than the recombination time itself.[31,32] Generally, shorter coherence leads to slower dynamics, as exemplified by the quantum Zeno effect in which the dynamics ceases in the limit of infinitely fast decoherence.[76−78]

To explore further the origin of the pure-dephasing process in the three systems under consideration, we computed the unnormalized autocorrelation functions (un-ACF) of the fluctuations of the HOMO−LUMO energy gaps (inset of Figure 5). Under the cumulant approximation, the dephasing function is computed by integrating un-ACF. A greater initial value of un-ACF and its slower decay favor faster dephasing.[75] All three ACFs exhibit similar decay, taking several hundred femtoseconds. The differences arise in the initial value. These are nearly identical for pristine $MAPbI_3$ and the undoped GB. Although the GB activates more phonon modes (Figure 4), it also decreases the gap (Figure 2). The two effects cancel each other, maintaining the same amplitude of gap fluctuation and the rate of elastic electron−phonon scattering. In contrast, the initial value of un-ACF for the doped GB is much larger compared to the other two systems (inset in Figure 5). This is rationalized by participation of many modes with high intensities (Figure 4c). As a result, the loss of quantum coherence accelerates (Figure 5), and the electron−hole recombination dynamics slows down (Figure 6).

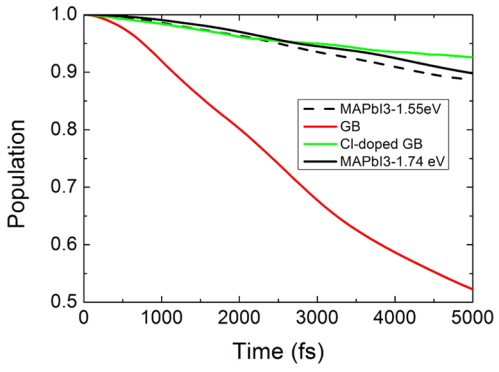

Figure 6. Electron−hole recombination dynamics in $MAPbI_3$, Σ5 (012) GB, and Cl-doped Σ5 (012) GB. The Σ5 (012) GB system shows faster decay compared to pristine $MAPbI_3$, due to larger NA coupling and longer coherence time. In contrast, the Cl-doped Σ5 (012) GB system demonstrates slower decay compared to pristine $MAPbI_3$, stemming from smaller NA coupling and shorter coherence time. The time scales summarized in Table 1 show good agreement with experiment.

DOI: 10.1021/jacs.6b00645
J. Am. Chem. Soc. 2016, 138, 3884−3890

3.4. Electron−Hole Recombination Dynamics. The data shown in Figure 6 are most important from the practical point of view. They show that, on the one hand, introduction of a GB greatly accelerates charge losses due to nonradiative electron−hole recombination, and that, on the other hand, Cl doping of the GB restores the recombination rate recorded for pristine $MAPbI_3$. The conclusion holds regardless of whether the calculated energy gap of 1.74 eV or the lowest of the experimentally determined[65] gaps of 1.55 eV is used. The electron−hole recombination time scales summarized in Table 1 were obtained by fitting the data in Figure 5 to the short-time linear approximation to the exponential decay. The electron−hole recombination times belong to the lower end of the 40−300 ps experimental range[31,32] and agree well with the previous theoretical calculations.[35] Because of the necessarily small size of the simulation cells, one expects that the electron−phonon coupling strengths and the charge recombination rates are overestimated. The extremely long time scales reported in other experiments,[12,26,79] extending to hundreds of nanoseconds, are attributed to charge-diffusion processes taking place over much longer spatial distances than those available to direct time-domain ab initio simulation.

The observed changes in the electron−hole recombination rate upon GB formation and GB doping are rationalized by the trends in the values of the energy gap, NA coupling, and pure-dephasing time (Table 1). The analysis of the gaps and coupling is presented in section 3.2. The sources of pure dephasing are considered in detail in section 3.3. Introduction of a GB decreases the gap and increases the coupling, leading to faster recombination. GB doping decreases both the coupling and the pure-dephasing time, making the recombination longer. The recombination times for the ideal system and the doped GB are similar, because acceleration due to decreased bandgap is offset by deceleration due to shorter coherence. These results rationalize a wide range of experimental observations on the influence of microstructure on excited-state lifetimes,[25−27] extend our previous research on dopant control of electron−hole recombination,[35,54] and serve to explain important experiments, indicating that Cl doping can greatly increase the conversion efficiency of perovskite solar cells.[1,9]

4. CONCLUSIONS

The nonradiative electron−hole recombination in methylammonium lead halide perovskites, with and without grain boundaries and chlorine doping, was investigated by nonadiabatic molecular dynamics combined with time-domain density functional theory. The recombination constitutes a major pathway of charge and energy losses in these materials, in particular limiting the photon-to-electron conversion efficiency in perovskite solar cells. The simulations clarify the long-term literature debate on whether grain boundaries are benign or detrimental to the solar cells performance. The simulations show that grain boundaries significantly increase the electron−hole recombination rate, while boundary doping with chlorines notably reduces the rate. The presented analysis establishes detailed mechanisms for these effects. The obtained results are rationalized at the atomistic level by changes in the nonadiabatic electron−phonon coupling, the bandgap, and the phonon-induced loss of coherence in the electronic subsystem. Grain boundaries reduce the bandgap and increase the coupling, thereby accelerating the nonradiative charge recombination. Chlorine doping of the boundaries decreases the coupling and increases coherence loss, thereby slowing the recombination down. The study highlights the importance of quantum coherence and electron-vibrational interactions in the excited-state dynamics of perovskite-based materials. The research presented in this paper advances our understanding of the key factors influencing and controlling the performance of hybrid organic−inorganic perovskite solar cells.

AUTHOR INFORMATION

Corresponding Authors

*runlong@bnu.edu.cn

*prezhdo@usc.edu

Notes

The authors declare no competing financial interest.

ACKNOWLEDGMENTS

R.L. is grateful to the National Science Foundation of China (Grant No. 21573022) and the Science Foundation Ireland SIRG Program (Grant No. 11/SIRG/E2172). O.V.P. acknowledges support of the U.S. Department of Energy, Grant No. DE-SC0014429.

REFERENCES

(1) Zhou, H.; Chen, Q.; Li, G.; Luo, S.; Song, T.-b.; Duan, H.-S.; Hong, Z.; You, J.; Liu, Y.; Yang, Y. *Science* **2014**, *345*, 542.

(2) Yan, K.; Long, M.; Zhang, T.; Wei, Z.; Chen, H.; Yang, S.; Xu, J. *J. Am. Chem. Soc.* **2015**, *137*, 4460.

(3) Lee, M. M.; Teuscher, J.; Miyasaka, T.; Murakami, T. N.; Snaith, H. J. *Science* **2012**, *338*, 643.

(4) Liu, D.; Yang, J.; Kelly, T. L. *J. Am. Chem. Soc.* **2014**, *136*, 17116.

(5) Im, J.-H.; Luo, J.; Franckevičius, M.; Pellet, N.; Gao, P.; Moehl, T.; Zakeeruddin, S. M.; Nazeeruddin, M. K.; Grätzel, M.; Park, N.-G. *Nano Lett.* **2015**, *15*, 2120.

(6) Gonzalez-Pedro, V.; Juarez-Perez, E. J.; Arsyad, W.-S.; Barea, E. M.; Fabregat-Santiago, F.; Mora-Sero, I.; Bisquert, J. *Nano Lett.* **2014**, *14*, 888.

(7) Zuo, L.; Gu, Z.; Ye, T.; Fu, W.; Wu, G.; Li, H.; Chen, H. *J. Am. Chem. Soc.* **2015**, *137*, 2674.

(8) Liu, Y.; Hong, Z.; Chen, Q.; Chang, W.; Zhou, H.; Song, T.-B.; Young, E.; Yang, Y.; You, J.; Li, G.; Yang, Y. *Nano Lett.* **2015**, *15*, 662.

(9) Edri, E.; Kirmayer, S.; Henning, A.; Mukhopadhyay, S.; Gartsman, K.; Rosenwaks, Y.; Hodes, G.; Cahen, D. *Nano Lett.* **2014**, *14*, 1000.

(10) Horváth, E.; Spina, M.; Szekrényes, Z.; Kamarás, K.; Gaal, R.; Gachet, D.; Forró, L. *Nano Lett.* **2014**, *14*, 6761.

(11) Jeon, N. J.; Noh, J. H.; Yang, W. S.; Kim, Y. C.; Ryu, S.; Seo, J.; Seok, S. I. *Nature* **2015**, *517*, 476.

(12) Guo, Z.; Manser, J. S.; Wan, Y.; Kamat, P. V.; Huang, L. *Nat. Commun.* **2015**, *6*, 7471.

(13) Dong, Q.; Fang, Y.; Shao, Y.; Mulligan, P.; Qiu, J.; Cao, L.; Huang, J. *Science* **2015**, *347*, 967.

(14) Stranks, S. D.; Eperon, G. E.; Grancini, G.; Menelaou, C.; Alcocer, M. J. P.; Leijtens, T.; Herz, L. M.; Petrozza, A.; Snaith, H. J. *Science* **2013**, *342*, 341.

(15) Xing, G.; Mathews, N.; Sun, S.; Lim, S. S.; Lam, Y. M.; Grätzel, M.; Mhaisalkar, S.; Sum, T. C. *Science* **2013**, *342*, 344.

(16) Zhang, Q.; Ha, S. T.; Liu, X.; Sum, T. C.; Xiong, Q. *Nano Lett.* **2014**, *14*, 5995.

(17) Zhu, H.; Fu, Y.; Meng, F.; Wu, X.; Gong, Z.; Ding, Q.; Gustafsson, M. V.; Trinh, M. T.; Jin, S.; Zhu, X. Y. *Nat. Mater.* **2015**, *14*, 636.

(18) Wong, A. B.; Lai, M.; Eaton, S. W.; Yu, Y.; Lin, E.; Dou, L.; Fu, A.; Yang, P. *Nano Lett.* **2015**, *15*, 5519.

(19) Jaeger, H. M.; Fischer, S.; Prezhdo, O. V. *J. Chem. Phys.* **2012**, *137*, 22A545.

(20) Chen, Y.-S.; Manser, J. S.; Kamat, P. V. *J. Am. Chem. Soc.* **2015**, *137*, 974.

DOI: 10.1021/jacs.6b00645
J. Am. Chem. Soc. 2016, 138, 3884−3890

(21) Kim, J. H.; Jo, Y.; Kim, J. H.; Jang, J. W.; Kang, H. J.; Lee, Y. H.; Kim, D. S.; Jun, Y.; Lee, J. S. *ACS Nano* **2015**, *9*, 11820.
(22) Song, Z. N.; Watthage, S. C.; Phillips, A. B.; Tompkins, B. L.; Ellingson, R. J.; Heben, M. J. *Chem. Mater.* **2015**, *27*, 4612.
(23) Yin, W.-J.; Shi, T.; Yan, Y. *Adv. Mater.* **2014**, *26*, 4653.
(24) Yin, W.-J.; Chen, H.; Shi, T.; Wei, S.-H.; Yan, Y. *Advanced Electronic Materials* **2015**, *1*, 1500044.
(25) Bischak, C. G.; Sanehira, E. M.; Precht, J. T.; Luther, J. M.; Ginsberg, N. S. *Nano Lett.* **2015**, *15*, 4799.
(26) de Quilettes, D. W.; Vorpahl, S. M.; Stranks, S. D.; Nagaoka, H.; Eperon, G. E.; Ziffer, M. E.; Snaith, H. J.; Ginger, D. S. *Science* **2015**, *348*, 683.
(27) Tosun, B. S.; Hillhouse, H. W. *J. Phys. Chem. Lett.* **2015**, *6*, 2503.
(28) Nie, W.; Tsai, H.; Asadpour, R.; Blancon, J.-C.; Neukirch, A. J.; Gupta, G.; Crochet, J. J.; Chhowalla, M.; Tretiak, S.; Alam, M. A.; Wang, H.-L.; Mohite, A. D. *Science* **2015**, *347*, 522.
(29) Xiao, Z.; Dong, Q.; Bi, C.; Shao, Y.; Yuan, Y.; Huang, J. *Adv. Mater.* **2014**, *26*, 6503.
(30) Runge, E.; Gross, E. K. U. *Phys. Rev. Lett.* **1984**, *52*, 997.
(31) Marchioro, A.; Teuscher, J.; Friedrich, D.; Kunst, M.; van de Krol, R.; Moehl, T.; Gratzel, M.; Moser, J.-E. *Nat. Photonics* **2014**, *8*, 250.
(32) Stamplecoskie, K. G.; Manser, J. S.; Kamat, P. V. *Energy Environ. Sci.* **2015**, *8*, 208.
(33) Yang, Y.; Ostrowski, D. P.; France, R. M.; Zhu, K.; van de Lagemaat, J.; Luther, J. M.; Beard, M. C. *Nat. Photonics* **2016**, *10*, 53.
(34) Yang, Y.; Yang, M. J.; Li, Z.; Crisp, R.; Zhu, K.; Beard, M. C. *J. Phys. Chem. Lett.* **2015**, *6*, 4688.
(35) Liu, J.; Prezhdo, O. V. *J. Phys. Chem. Lett.* **2015**, *6*, 4463.
(36) Jasper, A. W.; Nangia, S.; Zhu, C.; Truhlar, D. G. *Acc. Chem. Res.* **2006**, *39*, 101.
(37) Tully, J. C. *J. Chem. Phys.* **1990**, *93*, 1061.
(38) Craig, C. F.; Duncan, W. R.; Prezhdo, O. V. *Phys. Rev. Lett.* **2005**, *95*, 163001.
(39) Fischer, S. A.; Habenicht, B. F.; Madrid, A. B.; Duncan, W. R.; Prezhdo, O. V. *J. Chem. Phys.* **2011**, *134*, 024102.
(40) Akimov, A. V.; Prezhdo, O. V. *J. Chem. Theory Comput.* **2013**, *9*, 4959.
(41) Akimov, A. V.; Prezhdo, O. V. *J. Chem. Theory Comput.* **2014**, *10*, 789.
(42) Prezhdo, O. V. *J. Chem. Phys.* **1999**, *111*, 8366.
(43) Parandekar, P. V.; Tully, J. C. *J. Chem. Phys.* **2005**, *122*, 094102.
(44) Bittner, E. R.; Rossky, P. J. *J. Chem. Phys.* **1995**, *103*, 8130.
(45) Schwartz, B. J.; Bittner, E. R.; Prezhdo, O. V.; Rossky, P. J. *J. Chem. Phys.* **1996**, *104*, 5942.
(46) Zhu, C. Y.; Nangia, S.; Jasper, A. W.; Truhlar, D. G. *J. Chem. Phys.* **2004**, *121*, 7658.
(47) Mukamel, S. *Principles of Nonlinear Optical Spectroscopy*; Oxford University Press: New York, 1995.
(48) Long, R.; Prezhdo, O. V. *Nano Lett.* **2015**, *15*, 4274.
(49) Long, R.; Prezhdo, O. V. *Nano Lett.* **2014**, *14*, 3335.
(50) Long, R.; English, N. J.; Prezhdo, O. V. *J. Am. Chem. Soc.* **2013**, *135*, 18892.
(51) Long, R.; English, N. J.; Prezhdo, O. V. *J. Am. Chem. Soc.* **2012**, *134*, 14238.
(52) Long, R.; Prezhdo, O. V. *J. Am. Chem. Soc.* **2011**, *133*, 19240.
(53) Long, R.; Prezhdo, O. V. *J. Am. Chem. Soc.* **2014**, *136*, 4343.
(54) Long, R.; Prezhdo, O. V. *ACS Nano* **2015**, *9*, 11143.
(55) Akimov, A. V.; Asahi, R.; Jinnouchi, R.; Prezhdo, O. V. *J. Am. Chem. Soc.* **2015**, *137*, 11517.
(56) Akimov, A. V.; Prezhdo, O. V. *J. Am. Chem. Soc.* **2014**, *136*, 1599.
(57) Akimov, A. V.; Muckerman, J. T.; Prezhdo, O. V. *J. Am. Chem. Soc.* **2013**, *135*, 8682.
(58) Hyeon-Deuk, K.; Prezhdo, O. V. *Nano Lett.* **2011**, *11*, 1845.
(59) Kresse, G.; Furthmüller, J. *Phys. Rev. B: Condens. Matter Mater. Phys.* **1996**, *54*, 11169.
(60) Perdew, J. P.; Burke, K.; Ernzerhof, M. *Phys. Rev. Lett.* **1996**, *77*, 3865.
(61) Blöchl, P. E. *Phys. Rev. B: Condens. Matter Mater. Phys.* **1994**, *50*, 17953.
(62) Mosconi, E.; Amat, A.; Nazeeruddin, M. K.; Gratzel, M.; De Angelis, F. *J. Phys. Chem. C* **2013**, *117*, 13902.
(63) Even, J.; Pedesseau, L.; Jancu, J.-M.; Katan, C. *J. Phys. Chem. Lett.* **2013**, *4*, 2999.
(64) Grimme, S. *J. Comput. Chem.* **2006**, *27*, 1787.
(65) Stoumpos, C. C.; Malliakas, C. D.; Kanatzidis, M. G. *Inorg. Chem.* **2013**, *52*, 9019.
(66) Mosconi, E.; Quarti, C.; Ivanovska, T.; Ruani, G.; De Angelis, F. *Phys. Chem. Chem. Phys.* **2014**, *16*, 16137.
(67) Leguy, A. M. A.; Frost, J. M.; McMahon, A. P.; Sakai, V. G.; Kockelmann, W.; Law, C.; Li, X.; Foglia, F.; Walsh, A.; O'Regan, B. C.; Nelson, J.; Cabral, J. T.; Barnes, P. R. F. *Nat. Commun.* **2015**, *6*, 7124.
(68) Bakulin, A. A.; Selig, O.; Bakker, H. J.; Rezus, Y. L. A.; Müller, C.; Glaser, T.; Lovrincic, R.; Sun, Z.; Chen, Z.; Walsh, A.; Frost, J. M.; Jansen, T. L. C. *J. Phys. Chem. Lett.* **2015**, *6*, 3663.
(69) Quarti, C.; Mosconi, E.; Ball, J. M.; D'Innocenzo, V.; Tao, C.; Pathak, S.; Snaith, H. J.; Petrozza, A.; De Angelis, F. *Energy Environ. Sci.* **2016**, *9*, 155.
(70) Umebayashi, T.; Asai, K.; Kondo, T.; Nakao, A. *Phys. Rev. B: Condens. Matter Mater. Phys.* **2003**, *67*, 155405.
(71) Mosconi, E.; Amat, A.; Nazeeruddin, M. K.; Grätzel, M.; De Angelis, F. *J. Phys. Chem. C* **2013**, *117*, 13902.
(72) Umari, P.; Mosconi, E.; De Angelis, F. *Sci. Rep.* **2014**, *4*, 4467.
(73) Brivio, F.; Butler, K. T.; Walsh, A.; van Schilfgaarde, M. *Phys. Rev. B: Condens. Matter Mater. Phys.* **2014**, *89*, 155204.
(74) Quarti, C.; Grancini, G.; Mosconi, E.; Bruno, P.; Ball, J. M.; Lee, M. M.; Snaith, H. J.; Petrozza, A.; Angelis, F. D. *J. Phys. Chem. Lett.* **2014**, *5*, 279.
(75) Akimov, A. V.; Prezhdo, O. V. *J. Phys. Chem. Lett.* **2013**, *4*, 3857.
(76) Kilina, S. V.; Neukirch, A. J.; Habenicht, B. F.; Kilin, D. S.; Prezhdo, O. V. *Phys. Rev. Lett.* **2013**, *110*, 180404.
(77) Bray, A. J.; Moore, M. A. *Phys. Rev. Lett.* **1982**, *49*, 1545.
(78) Prezhdo, O. V. *Phys. Rev. Lett.* **2000**, *85*, 4413.
(79) Tian, W.; Zhao, C.; Leng, J.; Cui, R.; Jin, S. *J. Am. Chem. Soc.* **2015**, *137*, 12458.

DOI: 10.1021/jacs.6b00645
J. Am. Chem. Soc. 2016, 138, 3884−3890